Fast Surrogate Modeling using Dimensionality Reduction in Model Inputs and Field Output: Application to Additive Manufacturing

Manav Vohra[1], Paromita Nath[1], Sankaran Mahadevan[1], Yung-Tsun Tina Lee[2],

[1]Department of Civil and Environmental Engineering
Vanderbilt University
Nashville, TN 37235

[2]Systems Integration Division, Engineering Laboratory
National Institute of Standards and Technology (NIST)
Gaithersburg, MD, 20899

Corresponding Author: Sankaran Mahadevan
Department of Civil and Environmental Engineering
Vanderbilt University
272 Jacobs Hall, VU Mailbox: PMB 351831
Nashville, TN 37235

Phone: (615) 322-3040
Fax: (615) 343-3773
Email: sankaran.mahadevan@vanderbilt.edu

Submitted to: *Reliability Engineering & System Safety*
February 2019

Abstract

A novel approach to surrogate modeling motivated by recent advancements in parameter dimension reduction is proposed. Specifically, the approach aims to speed-up surrogate modeling for mapping multiple input variables to a field quantity of interest. Computational efficiency is accomplished by first identifying principal components (PC) and corresponding features in the output field data. A map from inputs to each feature is considered, and the active subspace (AS) methodology is used to capture their relationship in a low-dimensional subspace in the input domain. Thus, the PCAS method accomplishes dimension reduction in the input as well as the output. The method is demonstrated on a realistic problem pertaining to variability in residual stress in an additively manufactured component due to the stochastic nature of the process variables and material properties. The resulting surrogate model is exploited for uncertainty propagation, and identification of stress hotspots in the part. Additionally, the surrogate model is used for global sensitivity analysis to quantify relative contributions of the uncertain inputs to stress variability. Our findings based on the considered application are indicative of enormous potential for computational gains in such analyses, especially in generating training data, and enabling advancements in control and optimization of additive manufacturing processes.

Keywords: Surrogate model, dimension reduction, principal components, active subspace, additive manufacturing, residual stress

1 Introduction

The field of uncertainty quantification (UQ) can be broadly categorized into two classes of problems, namely, the *forward* problem and the *inverse* problem. The former involves propagating the uncertainty associated with model inputs to the output, whereas, the latter involves model calibration against the available set of measurements. Both forward and inverse problems typically require tens of thousands of model predictions at samples in the input space. Therefore, UQ becomes remarkably challenging in situations where simulating the model is computationally intensive. Other pertinent analyses in computational science such as sensitivity analysis, optimization under uncertainty, risk and reliability assessment also require a large number of model predictions and thus offer similar challenges. Moreover, in complex systems, it is commonplace that a multivariate output which can also be a field quantity (exhibits spatial dependence) or a stochastic process (exhibits temporal dependence) is a function of a large set of variables in the input domain. It is not surprising therefore, that numerous research efforts especially in UQ and reliability analysis have focused on efficient ways to map the set of model inputs to the output. These efforts have mainly resulted in techniques for constructing a so-called *surrogate model* that effectively aims to capture the dependence of a model output on its inputs.

As discussed above, a surrogate model can offer a significant computational advantage in mapping a set of model inputs to the output especially in situations involving intensive model simulations. However, constructing a reasonably accurate surrogate itself can be computationally demanding due to the need to generate training points using the original physics model. For instance, estimation of coefficients of a polynomial chaos expansion (PCE) [1–3], can be computationally demanding in large-dimensional applications despite recent development of sparse grids [4, 5] and basis adaptive methods [6, 7]. Similarly, in the case of Gaussian Process (GP) [8] surrogate modeling, computing the inverse of the covariance matrix becomes challenging in large dimensions. Additionally, the number of tuning parameters associated with the correlation function also increase with dimensions thereby limiting the applicability of GPs in large-dimensional applications. In the case of support vector machines (SVMs) [9] and neural networks (NNs) [10], commonly used machine

learning models for regression as well as classification, the accuracy is largely dependent on the data used to train them. Hence, their applicability is limited in situations involving sparse and noisy training data.

Traditional methods for surrogate modeling have mainly focused on gains in efficiency by reducing the dimensionality in either the input space or the output space. Dimension reduction in the input space aims to reduce the training effort using sparse grids [11–14], projection to a sparse orthogonal basis (e.g. PCE, proper orthogonal decomposition (POD) or principal component analysis (PCA), Karhunen-Loéve Expansion) [15–17] or a combination of both strategies (e.g. sparse pseudospectral approximation) [7, 18–20]. On the other hand, dimension reduction in the output space has been accomplished using spectral decomposition to capture dominant modes or principal directions in the output data represented in the form of a matrix (e.g. PCA) [21–24]. Additionally, methods such as co-kriging [25] have also been used for the case of multivariate outputs. However, co-kriging approaches can be computationally demanding for large-dimensional field quantities of interest [26]. Recent efforts in this direction have focused on gradient-based techniques for subspace computation for dimension reduction in situations involving multivariate outputs [27, 28]. These efforts aim to extend the applicability of active subspace methods [29, 30] typically applied to scalar-valued functions.

In this work, we present a novel approach aimed at combining dimension reduction in the output space with dimension reduction in the input space. Specifically, PCA is exploited to extract key features in the output field quantity of interest. Then, we discover a low-dimensional structure in the relationship between representative features of the output and the set of inputs using the active subspace methodology [30]. The proposed methodology is referred to as the PCAS method in this work as it combines principal component analysis (PCA) with active subspaces (AS). Thus, the proposed methodology aims to *compound* computational gains by constructing a low-dimensional relationship between uncertain variables in the input space and representative features in a low-dimensional output space.

The PCAS method is applied to a multiphysics problem wherein a surrogate is constructed for an expensive thermo-mechanical finite element model (FEM) to enable uncertainty propagation from a set of inputs (process variables and material properties) to a field

output (residual stress) in a mechanical component fabricated using an additive manufacturing process. Additionally, the surrogate model is used to perform a global sensitivity analysis (GSA) to quantify relative contributions of individual uncertain variables to variability in residual stress. The surrogate model is further exploited to perform a reliability analysis of the component. Traditional approaches for reliability analysis in the field of additive manufacturing have predominantly relied on trial-and-error based approaches and are therefore limited in terms of scope and applicability. Tremendous scope for computational gains is demonstrated for this purpose using the proposed approach in this work. Specifically, the resulting surrogate, constructed using a sparse set of realizations of the expensive physics model is shown to reconstruct the field quantity of interest (residual stress) with reasonable accuracy. The output is undoubtedly high-dimensional since it is a field quantity. It must also be highlighted that each run of the physics model requires approximately 30 minutes as discussed further below. The application in this work considers 12 uncertain inputs including process variables and material properties. Exploring the 12-dimensional parameter space for the aforementioned analyses (uncertainty propagation, GSA, reliability) would require tens of thousands of model runs which essentially precludes us from using the original model for this purpose. Considering the underlying computational effort, the input space can also be regarded as high-dimensional. A generalized framework of the proposed methodology is presented which motivates its use for such applications and potential extension to higher-dimensional problems.

Residual stress develops during additive manufacturing due to the presence of steep thermal gradients as well as physical constraints in the part which adversely affect its mechanical properties, geometry, and shape [31–33]. In fact, residual stress in addition to porosity is one of the concerns in additively manufactured (AM) components [34], and has significantly inhibited rapid certification as well as standardization of the certification process due to post processing involving machining and heat treatment [35]. Several recent investigations [36–38] have focused on developing thermo-mechanical models to better understand the development of residual stress and optimize the microstructure as well as the manufacturing process parameters accordingly. However, since simulations are intensive and models require a large amount of calibration data, the progress has so far been limited by the availability of compu-

tational and experimental resources. Through this study, we aim to demonstrate an effective strategy based on surrogate modeling that could accelerate material selection, microstructure design, and process control and optimization for controlling the evolution residual stress during additive manufacturing.

Residual stress in the part is computed for a single scan of an electron beam in the Electron Beam Melting (EBM) process considered in this work. Simulations are performed using a finite element thermo-mechanical model in Abaqus in this work. More specifically, the FEM includes a thermal model that simulates the thermal response of the part. Part thermal response is then used as an input to a mechanical model that predicts residual stress at the end of a cooling phase. For a given set of process conditions and material properties, the thermal model requires approximately 20 minutes to generate the temperature field and the mechanical model takes approximately 10 minutes to estimate the residual stress in the part. Therefore, one realization of the output field of interest using the FEM requires approximately 30 minutes. In order to perform reliability analysis using sampling techniques, $\mathcal{O}(10^4 - 10^5)$ realizations are typically required for reasonable accuracy. Therefore, it is not practical to rely on the FEM for this purpose. Additionally, conventional approaches for surrogate modeling would require a large amount of computational resources for the purpose of training as mentioned earlier. A parametric random field description is a possibility for output dimension reduction by representing the output with a small number of parameters. However, such an approximation could be difficult and erroneous in the case of a non-stationary output field wherein the covariance between any two points in the field is dependent on their spatial or temporal location in addition to its difference. Instead, we aim to exploit the structure in the output data by identifying important directions or principal components in the field. This approach allows us to select an optimal number of features required to re-construct the field with reasonable accuracy and computational effort.

The main highlights of this paper are as follows: (1) A computationally efficient approach is developed for constructing a surrogate model for problems where both input and output are high-dimensional using sparse training data. In particular, the output is a field quantity. (2) Thermo-mechanical finite element modeling is pursued to simulate residual stress distribution in an additively manufactured part. (3) The surrogate model is used to perform uncertainty

propagation and global sensitivity analysis (GSA) to assess the relative importance of the material properties and manufacturing process parameters. (4) Finally, the surrogate model is used for the purpose of reliability analysis by estimating the probability that residual stress in the part exceeds a certain threshold.

The remainder of this paper is organized as follows: Section 2 outlines the proposed methodology for constructing the surrogate model including a brief background on the active subspace methodology used in this work. Section 3 details the finite element model used to generate stress data for building the surrogate model. Section 4 provides numerical results and discussion pertaining to the implementation of the methodology for surrogate construction, hotspot identification, GSA, and reliability analysis of the AM product. Finally, we summarize this study in Section 5.

2 Methodology

2.1 Random field discretization

Random field discretization is employed in the proposed method, and therefore a few preliminary comments are provided in this subsection. In this work, we consider a scenario where the model output is a spatially distributed quantity. The model inputs are considered as random variables and the output is regarded as a *random field* to account for spatial variability. A random field is essentially a collection of random quantities in space. The random quantity at any given point in space can be a scalar or a vector resulting in a univariate or a multivariate random field respectively. Model prediction at a specific point in continuous space is considered to be scalar (random variable) in this work. The corresponding random field representation is thus univariate and infinite-dimensional. Dimension reduction in the output space is accomplished through *discretization*, i.e., by representing by representing the random field in terms of a finite number of random variables. One commonly used method for random field discretization is the Karhunen-Loéve expansion (KLE) which employs a spectral decomposition in terms of eigenvalues and eigenfunctions of the autocovariance kernel of a random field. KLE is mainly applicable to Gaussian random fields although several studies have focused on enhancing its applicability to non-Gaussian fields [39–42]. To avoid

numerical issues pertaining to KLE, the autocovariance kernel associated with the field is required to be bounded, symmetric and positive semi-definite [43]. Therefore, the feasibility of the random field discretization is largely dependent on the choice of the numerical method for solving a suitable eigenvalue problem for a given application. Several methods such as functional principal component analysis (PCA) for time-dependent problems [44], the Nystrom method [45, 46] for integral eigenvalue problems, and the EOLE method [47] for complex geometries have been developed for this purpose.

The proposed approach relies on the feasibility of a random field discretization for a given application. While this requirement poses a limitation on its applicability, the main focus of this paper, which is to map a sparse set of representative random variables (from random field discretization) to a set of input variables in a low-dimensional subspace could be valuable in many applications. Such a map is referred to as a surrogate model in this work. Our approach for building a surrogate model is demonstrated on an engineering application from additive manufacturing. Although the methodology is demonstrated using a simple 2D uniform mesh, it is extensible to more complex geometries using the advanced numerical methods mentioned above. Note that even for a simple geometry, the UQ analyses and sensitivity studies discussed in this work would be intractable using the original physics model. Therefore, a surrogate model is needed to make the analyses computationally affordable.

2.2 The PCAS method

The PCAS method aims to construct a surrogate model that captures the relationship between a set of inputs that map to an output which is a field quantity. Building the surrogate model using this method is shown to be remarkably efficient by means of dimension reduction in the input as well as the output space. Dimension reduction in the field output is accomplished using PCA, and using active subspaces in the input space. Both PCA and active subspaces are well established and have been discussed in much detail in the literature. Therefore, we focus our efforts on providing details pertaining to the implementation of these ideas in this section and include references for further mathematical details. Additionally, we outline the underlying mathematical framework associated with active subspaces considering that it is a more recent development. The method is demonstrated for an additive

manufacturing process wherein the set of inputs correspond to process variables and material properties, and the output corresponds to a two-dimensional stress field in a cross-section of a component. Additional details pertaining to the AM process are provided in Section 3. In this section, we provide a general framework that can be easily adapted for such applications.

In the proposed methodology, we outline a two-step process to accomplish this. The first step involves dimension reduction in the output space that involves identification of principal directions or components in the dataset for the field of interest.The principal components constitute the so-called orthogonal space on which variables in the original physical domain are projected. We refer to these variables, projected onto the orthogonal space as 'features' in this work. Mathematically, each feature is an inner product of the field data and elements of a given principal direction. Hence, the number of features is equal to the number of principal directions used to reconstruct the field. In the second step, each feature is represented as a function of the inputs and a low-dimensional representation of the function is computed using the active subspace methodology outlined in [30]. To avoid unnecessary computations of the finite element model and thereby enhance the efficiency of the proposed method, the two steps are implemented in an iterative manner as discussed further below. In 2.2.1, we outline the strategy for computing the feature vector. In 2.2.2, we provide a brief background on active subspaces and outline the sequence of steps for surrogate construction for each feature. The proposed iterative procedure for constructing the surrogate is discussed in 2.2.4.

2.2.1 Output dimension reduction using PCA

As discussed earlier, the surrogate model in this work is used to reconstruct a field quantity for a given set of model inputs and parameters. The spatially varying field quantity, $\mathbf{S} = \mathbf{S}(\boldsymbol{x}, \boldsymbol{\theta})$ ($\boldsymbol{x}$: computational domain, $\boldsymbol{\theta}$: model inputs) is essentially obtained by simulating a physics-based model. It is assumed including in the application presented in this work in Section 3, that the numerical method (including the underlying scheme and discretization) used to simulate the model, results in a converged solution with reasonably small approximation errors. Additionally, the scheme is stable (bounded numerical errors) for the considered application. Numerical simulations of field quantities are typically performed using meshes or grids which transform a continuous field variable into a matrix, each element of which

corresponds to its value at a particular node of the mesh. Thus, for the purpose of outlining the mathematical details pertaining to the implementation of the proposed methodology, the 2-dimensional field is represented as a matrix as discussed further below.

We consider a field, $\mathbf{S}(\boldsymbol{\theta}) \in \mathbb{R}^{r \times c}$ evaluated on a 2-dimensional mesh of size $(r \times c)$ for a given set of inputs $\boldsymbol{\theta}$. Consider that the field data is available at N_s pseudorandom samples, drawn from the joint probability density function (PDF) of $\boldsymbol{\theta}$. A data matrix $\mathbf{X}$ is first constructed using the field data at N_s samples. Specifically, $\mathbf{X}$ has N_s rows and $(r \times c)$ columns. Thus, each row of $\mathbf{X}$ contains the matrix $\mathbf{S}$, reshaped as a long vector of size $(r \times c)$. Specific steps pertaining to the construction of the $\mathbf{X}$ are provided in Algorithm 1 (lines 3–11). A singular value decomposition SVD of the covariance matrix, $\mathbf{X}^\top\mathbf{X}$ is then performed to obtain an orthogonal matrix, $\mathbf{U}$ of size: $[(r \times c) * N_s])$. Note that since $\mathbf{X}^\top\mathbf{X}$ is symmetric positive semidefinite, performing an SVD is identical to performing a spectral or an eigenvalue decomposition. The columns of $\mathbf{U}$ contain eigenvectors or principal directions in the considered data. A matrix, $\mathcal{Z}$ with N_s rows, each representing a feature vector corresponding to a sample is obtained by multiplying the matrices, $\mathbf{X}$ and $\mathbf{U}$. The length of a feature vector or the number of columns in $\mathcal{Z}$ are thus equal to the number of eigenvectors (K) or columns in $\mathbf{U}$, sufficient for reconstructing the field $\mathbf{S}$ with reasonable accuracy. It must be noted each entry in $\mathbf{S}$ represents a feature in the physical space i.e. the value of a physical quantity at a particular point in the mesh. Entries in $\mathcal{Z} = (\mathbf{X}\mathbf{U}(:, 1:K))$ correspond to the features or variables in the physical space projected onto the orthogonal or latent space. The field $\mathbf{S}$ is essentially reconstructed by projecting the features back to the physical space by multiplying $\mathcal{Z}$ and the transpose of $\mathbf{U}$ since the latter is orthogonal. Since most of the information is captured by the dominant eigenvectors, $\mathbf{S}$ can be re-constructed with a reasonable amount of accuracy in a low-dimensional column space of $\mathbf{U}$. We adopt an iterative approach wherein the number of eigenvectors or components of $\mathbf{U}$ are increased by one at each iteration and the accuracy of the reconstructed field $\hat{\mathbf{S}}$ is assessed. Thus, the optimal number of components correspond to the reconstruction error $\varepsilon_{\mathcal{R}}^{\infty}$ being smaller than a desired threshold τ. The sequence of steps is outlined in Algorithm 1.

Algorithm 1 Determining the optimal number of components, K^* for reconstructing $\mathbf{S}$

Input: τ, $\mathbf{S}_i$'s, $\boldsymbol{\theta_i}$'s $(i = 1, 2, \ldots, N_s)$
Output: $\mathbf{U}^r$, K^*

procedure OUTPUT DIMENSION REDUCTION
    Construct the data matrix, $\mathbf{X}$:
    Set $k = 0$
    loop
        Reshape $\mathbf{S}_i \in \mathbb{R}^{r \times c}$ into a vector, $\boldsymbol{S}_{v,i} \in \mathbb{R}^{(r*c)\times 1}$
        $k = k + 1$
        $\mathbf{X}(k, :) = \boldsymbol{S}_{v,i}$
        if $k = N_s$ **then**
            break ▷ exit the loop when all N_s rows have been assigned
        end if
    end loop
    Perform a Singular Value Decomposition (SVD) on the covariance matrix, $\mathbf{X}^\top\mathbf{X}$:

$$\mathbf{X}^\top\mathbf{X} = \mathbf{U}\mathbf{W}\mathbf{V}^\top$$

    Optimize the number of components, K:
    Set $K = 1$
    loop
        Compute the feature matrix, $\mathcal{Z}$:

$$\mathcal{Z} = \mathbf{X}\mathbf{U}(:, 1 : K)$$

        Reconstruct the data matrix, $\mathbf{X}$ as $\hat{\mathbf{X}}$:

$$\hat{\mathbf{X}} = \mathcal{Z}\mathbf{U}(:, 1 : K)^\top$$

        Each row in $\hat{\mathbf{X}}$ corresponds to the field vector $\hat{\boldsymbol{S}}_{v,i}$
        Estimate the relative error, $\varepsilon^\infty_{\mathcal{R}}$ by comparing $\boldsymbol{S}_{v,i}$ and $\hat{\boldsymbol{S}}_{v,i}$ at each sample, i:

$$\varepsilon^\infty_{\mathcal{R}} = \max_i \frac{\|\boldsymbol{S}_{v,i} - \hat{\boldsymbol{S}}_{v,i}\|_\infty}{\|\boldsymbol{S}_{v,i}\|_\infty}, i = 1, 2, \ldots, N_s$$

        if $\varepsilon^\infty_{\mathcal{R}} < \tau$ **then**
            $K^* = K$ ▷ τ: specified tolerance
            $\mathbf{U}^r = \mathbf{U}(:, 1 : K^*)$
            break ▷ exit when optimal number of components (K^*) has been determined
        end if
        $K = K + 1$
    end loop
end procedure

At the end of the iterative procedure, a feature vector with K^* components is obtained for each $\boldsymbol{\theta_i}$. Dimension reduction in the output space is achieved in situations where $K^* < (r*c)$, where $(r * c)$ is the dimensionality of the column space of $\mathbf{U}$. In fact, smaller the ratio: $K^*/(r*c)$, larger the expected computational gains due to dimension reduction in the output

space. Therefore, the expected gains are problem dependent. For instance, in problems where the field of interest exhibits irregularities or discontinuities, significant dimension reduction using PCA will generally not be possible. The feature matrix, $\mathcal{Z}$ can be mathematically represented as follows:

$$\mathcal{Z} = \begin{pmatrix} \mathcal{Z}_{11} & \mathcal{Z}_{21} & \cdots & \mathcal{Z}_{K^*1} \\ \mathcal{Z}_{12} & \mathcal{Z}_{22} & \cdots & \mathcal{Z}_{K^*2} \\ \vdots & \vdots & \ddots & \vdots \\ \mathcal{Z}_{1N_s} & \mathcal{Z}_{2N_s} & \cdots & \mathcal{Z}_{K^*N_s} \end{pmatrix} \tag{1}$$

The data matrix in the right hand side (RHS) of (1) is used to construct an active subspace for each feature, $\mathcal{Z}_i$ $(i = 1, 2, \ldots, K^*)$ as discussed in the following section. Note that $\mathcal{Z}_{ij}$ denotes the j^{th} realization of the i^{th} feature, $\mathcal{Z}_i$.

2.2.2 Active subspace discovery

Each column in the feature matrix, $\mathcal{Z}$ corresponds to N_s realizations of a feature in the latent space. In other words, each column captures the variability in corresponding feature due to variability in inputs, $\boldsymbol{\theta}$ exhibited by N_s samples. A feature corresponding to the i^{th} column, $\mathcal{Z}_i = \mathcal{Z}_i(\boldsymbol{\theta})$ can thus be considered as a scalar valued function of the set of inputs, $\boldsymbol{\theta}$. An active subspace in the present context is a low-dimensional subspace in the input domain that effectively captures the variability in $\mathcal{Z}_i$ due to variations in $\boldsymbol{\theta}$. The set of inputs, $\boldsymbol{\theta}$ in the physical space are parameterized as canonical random variables, $\boldsymbol{\xi} \in \Omega \in \mathbb{R}^{N_\theta}$, where N_θ denotes the number of uncertain parameters referred to as the dimensionality of the parameter space. The active subspace is spanned by the dominant eigenvectors of a matrix, $\mathcal{C}$ comprising the derivative information of $\mathcal{Z}_i$ with respect to the components of $\boldsymbol{\xi}$. Note that a component ξ_k can be projected back to the physical space to its corresponding potential parameter, θ_k. The positive semi-definite matrix, $\mathcal{C}$ for the i^{th} feature is given as follows:

$$\mathcal{C}_i = \int_\Omega (\nabla_{\boldsymbol{\xi}} \mathcal{Z}_i)(\nabla_{\boldsymbol{\xi}} \mathcal{Z}_i)^\top dP_{\boldsymbol{\xi}}, \tag{2}$$

where $dP_{\boldsymbol{\xi}} = \pi_{\boldsymbol{\xi}} d\boldsymbol{\xi}$ and $\pi_{\boldsymbol{\xi}}$ denotes the joint PDF of $\boldsymbol{\xi}$. Note that $\mathcal{Z}_i$ is assumed to be differentiable and L^2 integrable in Ω_θ. The validity of this assumption is tested by comparing the field evaluated using the surrogate model with the same field evaluated using the original

model for the considered application in 4.1.1. Since the integral in (2) is multidimensional, the symmetric and positive semidefinite matrix $\mathcal{C}_i$ is approximated numerically in practice. Consider its sampling based estimate and associated eigenvalue decomposition as follows:

$$\mathcal{C}_i \approx \hat{\mathcal{C}}_i = \frac{1}{N}\sum_{l=1}^{N}(\nabla_{\boldsymbol{\xi}}\mathcal{Z}_i(\boldsymbol{\xi}_l))(\nabla_{\boldsymbol{\xi}}\mathcal{Z}_i(\boldsymbol{\xi}_l))^\top = \hat{\mathbf{W}}\hat{\boldsymbol{\Lambda}}\hat{\mathbf{W}}^\top. \tag{3}$$

The matrix $\hat{\mathbf{W}}$ comprises orthonormal eigenvectors as its columns, and $\hat{\boldsymbol{\Lambda}}$ is a diagonal matrix with eigenvalues arranged in descending order as its elements:

$$\lambda_1 \geq \lambda_2 \geq \cdots \geq \lambda_{N_\theta} \geq 0.$$

Dimension reduction is achieved by partitioning the eigenpairs about the j^{th} eigenvalue such that $\left(\frac{\lambda_j}{\lambda_{j+1}}\right) \gg 1$ as follows:

$$\hat{\mathbf{W}} = [\hat{\mathbf{W}}_1\ \hat{\mathbf{W}}_2], \quad \hat{\boldsymbol{\Lambda}} = \begin{bmatrix} \hat{\boldsymbol{\Lambda}}_1 & \\ & \hat{\boldsymbol{\Lambda}}_2. \end{bmatrix} \tag{4}$$

The column space of $\hat{\mathbf{W}}_1$ constitutes the active subspace, and $\hat{\boldsymbol{\Lambda}}_1$ is the corresponding diagonal matrix with its elements: $\{\lambda_1, \ldots, \lambda_{N_j}\}$, where N_j is the number of columns or eigenvectors in $\hat{\mathbf{W}}_1$. $\mathcal{Z}_i(\boldsymbol{\theta})$, a function of N_θ independent variables is transformed as $G_i(\boldsymbol{\eta})$, a function of j independent variables since $\boldsymbol{\eta} = \hat{\mathbf{W}}_1^\top\boldsymbol{\xi} \in \mathbb{R}^{N_j}$. In other words, $G_i(\boldsymbol{\eta})$ assumes the same set of values as $\mathcal{Z}_i(\boldsymbol{\theta})$, i.e. $G_i(\boldsymbol{\eta}) = \mathcal{Z}_i(\boldsymbol{\theta})$. However, the former is a function of the so-called *active variables* $\boldsymbol{\eta}$, whereas the latter is a function of the physical variables $\boldsymbol{\theta}$.

From (3), it is clear that the computational effort needed to construct $\mathcal{C}_i$ is directly proportional to the number of samples, N. A regression-based approach outlined in [48] and adapted from Algorithm 1.2 in [30] is used to estimate the gradients of $\mathcal{Z}_i$, required to compute the elements of $\mathcal{C}_i$. In this approach, the gradient is estimated using linear-regression fits to a set of available model evaluations. Specifically, the methodology presented in [48] increases the number of model evaluations in an iterative manner based on convergence of dominant eigenvectors of $\mathcal{C}$. Therefore, gradient estimation approach in [48] essentially aims to enhance the efficiency of Algorithm 1.2 in [30] by using an iterative approach and thereby avoiding unnecessary model evaluations. The iterative approach is not included in this paper in the interest of brevity and we encourage interested readers to look into the aforementioned references for further details.

Gradient estimation using the regression approach is expected to be computationally advantageous in situations where simulations are expensive and the model output does not exhibit large non-linearities or irregularities. An active area of research explores alternative techniques such as adjoint-based methods [49, 50], automatic differentiation [51], and regression-based estimation of gradients using quadratic fits [52]. However, exploring these advanced strategies is not the focus of this work and the proposed framework can be extended to incorporate them for the purpose of gradient estimation. Based on the results presented later in Section 4, the regression-based approach involving linear fits in an iterative manner as discussed, seems to be a reasonable choice for the considered application.

2.2.3 Surrogate in the active subspace

Dimension reduction in the input space using the active subspace methodology aims to accomplish computational gains in two ways: First, representative features of the output are expressed in terms of fewer independent variables (active variables) in the active subspace as $G_i(\boldsymbol{\eta})$. Second, the dependence of individual features on the active variables is approximated using a surrogate model $\hat{G}_i(\boldsymbol{\eta})$ in the active subspace. For a low-dimensional surrogate model (1 or 2 dimensions), a polynomial regression fit is often an adequate choice. However, for a relatively large dimensional active subspace, one could use a PCE or a GP. It is however critical to assess the surrogate model for its accuracy. The following algorithm provides a sequence of steps adapted from [30] to construct a surrogate model in the active subspace.

Algorithm 2 For constructing a surrogate model in the active subspace

1: **procedure** SURROGATE MODEL, $\hat{G}_i(\boldsymbol{\eta})$
2: Consider N available data points in the full space, $(\boldsymbol{\xi}_k, \mathcal{Z}_i(\boldsymbol{\xi}_k))$, $k = 1, \ldots, N$
3: For each $\boldsymbol{\xi}_k$, compute $\boldsymbol{\eta}_k = \mathbf{W}_1^\top \boldsymbol{\xi}_k$ (Note: $G_i(\boldsymbol{\eta}_k) = \mathcal{Z}_i(\boldsymbol{\xi}_k)$)
4: Fit a regression surface, $\hat{G}_i(\boldsymbol{\eta})$ to approximate $G_i(\boldsymbol{\eta})$ using the data points, $(\boldsymbol{\xi}_k, G_i(\boldsymbol{\eta}_k))$
5: Note that the overall approximation is: $\mathcal{Z}_i(\boldsymbol{\xi}) \approx \hat{G}_i(\mathbf{W}_1^\top \boldsymbol{\xi})$
6: **end procedure**

To sum up, an active subspace is computed for each dominant feature, $\mathcal{Z}_i$ and a corresponding surrogate fit, $\hat{\mathcal{Z}}_i$ is performed. Therefore, a total of K^* surrogate models are

constructed to map the set of inputs $\boldsymbol{\theta}$ in the physical space to the field in the output space. Therefore, at the end of the two-step process, dimension reduction in the output space is $\mathbb{R}^{(r*c)} \rightarrow \mathbb{R}^{K^*}$, and dimension reduction in the input space is $\mathbb{R}^{N_\theta} \rightarrow \mathbb{R}^{N_{\boldsymbol{\eta},\max}}$; where $N_{\boldsymbol{\eta},\max}$ corresponds to the surrogate model with the largest dimensionality in $\boldsymbol{\eta}$.

In the context of expensive multiphysics models that need to be used to generate training points for the surrogate model, it is desirable to minimize the number of training points. Therefore an iterative procedure for constructing the surrogate model is discussed in 2.2.4.

2.2.4 Iterative procedure for surrogate construction

As a first step, we construct a validation dataset using the expensive multiphysics model for testing the accuracy of the surrogate model. An initial set realizations of the output field is generated at N_0 samples (drawn from the joint PDF of $\boldsymbol{\theta}$) using the original model. The optimal number of components (K^0) or representative features ($\mathcal{Z}_i^0$, $i = 1, \ldots, K^0$) are then determined for the initial dataset using Algorithm 1. A map from $\boldsymbol{\xi}$ to each feature $\mathcal{Z}_i^0$ is approximated by a surrogate model: $\mathcal{Z}_i^0(\boldsymbol{\xi}) \approx \hat{G}_i(\boldsymbol{\eta})$ in the active subspace using the methodology presented in 2.2.2. The output field is reconstructed using surrogate prediction for each feature $\mathcal{Z}_i^0$. Finally, to assess the accuracy of the resulting surrogate, we estimate the surrogate fitting error ($\varepsilon_0^{\text{fit}}$) and validation error ($\varepsilon_0^{\text{val}}$). The output field is reconstructed at the training points to estimate the former and at an independently generated set of realizations of the field using the multiphysics model to estimate the latter. The mathematical expression for the two errors is given as follows:

$$\varepsilon_0^{\text{fit,val}} = \frac{1}{N_0^{\text{fit,val}}} \sum_{i=1}^{N_0^{\text{fit,val}}} \frac{\|\mathbf{S}_0 - \hat{\mathbf{S}}_0\|_2}{\|\mathbf{S}_0\|_2}, \tag{5}$$

where N_0^{fit} and N_0^{val} denote the number of samples used for estimating the fitting error and the validation error respectively; $\mathbf{S}_0$ and $\hat{\mathbf{S}}_0$ denote the output field simulated using the original model and the surrogate model respectively. Note that the subscript '0' indicates that these variables correspond to the initial set of computations. A new set of realizations for the residual stress field is generated at each subsequent iteration and augmented with the existing dataset. The two-step process is repeated until both $\varepsilon_0^{\text{fit}}$ and $\varepsilon_0^{\text{val}}$ are found to be smaller than a prescribed tolerance. In other words, convergence is established once the

reconstructed field is observed to be accurate within a certain threshold. The sequence of steps associated with the iterative procedure for building the surrogate model is provided in Algorithm 3.

Algorithm 3 Iterative strategy for surrogate modeling using the PCAS method

Input: Nominal values and intervals for each component of $\boldsymbol{\theta}$, Error threshold: τ_s

Output: K^*, $\hat{G}_i^*(\boldsymbol{\eta})$ $(i = 1, \ldots, K^*)$

1: **procedure** PCAS METHODOLOGY
2: Draw an initial set of N_0 samples from the joint PDF $\pi_{\boldsymbol{\theta}}$
3: Generate model realizations of the residual stress field at these N_0 samples
4: Determine optimal number of components K^0 using Algorithm 1
5: Discover an active subspace for each feature $\mathcal{Z}_i^0(\boldsymbol{\theta})$
6: Approximate $\mathcal{Z}_i^0(\boldsymbol{\theta})$ with a low-dimensional surrogate $\hat{G}_i^0(\boldsymbol{\eta})$
7: Reconstruct the output field $\hat{\mathbf{S}}_0$
8: Evaluate the relative errors: $\varepsilon_0^{\text{fit}}$ and $\varepsilon_0^{\text{val}}$ using (5)
9: **if** $(\varepsilon_0^{\text{fit}} < \tau_s$ AND $\varepsilon_0^{\text{val}} < \tau_s)$ **then**
10: $K^* = K^0$
11: $\hat{G}_i^*(\boldsymbol{\eta}) = \hat{G}_i^0(\boldsymbol{\eta})$
12: Proceed to Step 17
13: **end if**
14: Draw a new set of samples $\boldsymbol{\theta}^{\text{new}}$ from $\pi_{\boldsymbol{\theta}}$ and perform model evaluations at $\boldsymbol{\theta}^{\text{new}}$
15: Augment the new dataset with existing dataset for building the surrogate
16: Repeat Steps 4–9 and 14–15 until the 'if' condition is satisfied
17: **end procedure**

An overall flow diagram for the two-step process implemented at each iteration for the input and output dimension reduction is illustrated in Figure 1. Once dimension reduction for a given iteration is complete, the field is reconstructed using the sequence illustrated in Figure 2.

The proposed method is found to be remarkably effective in constructing an efficient surrogate model for the considered application involving a field output and expensive simu-

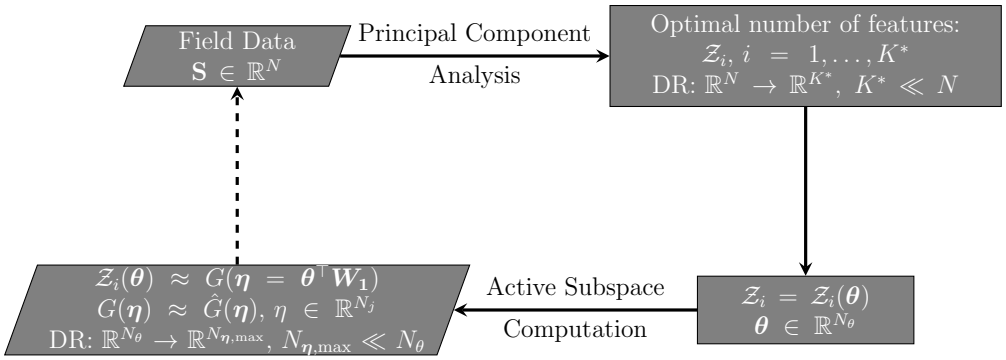

Figure 1: Flow diagram illustrating the sequence of steps and associated dimension reduction (DR) in the PCAS method.

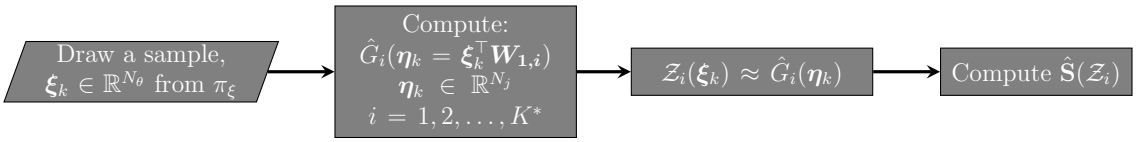

Figure 2: Flow diagram illustrating the sequence of steps for reconstructing the field of interest.

lations of the physics model based on the results presented later in Section 4. The method can be extended or adapted to other applications which could further help characterize its effectiveness in scenarios that are relatively more complex with regards to dimensionality and the stochastic nature of the field output.

3 Electron Beam Melting: Multiphysics Model

Electron beam melting (EBM) is an additive manufacturing process of fusing powder particles, layer-upon-layer, using an electron beam as the energy source. The process is typically used in the case of metals and its alloys. Multiple passes of a low power electron beam is used for heating and sintering the powder bed prior to selective melting. For the application problem in this study, we focus on the thermo-mechanical behavior of an AM part produced by the EBM process. For this purpose, we have developed a finite element-based thermal analysis model to simulate the thermal response of the part and a finite element-based mechanical model that uses the part's thermal response to estimate the residual stress in the

part at the end of the cooling phase. Note that the stress is computed at the end of a single pass of the electron beam. In this study, the two models are weakly coupled i.e. the temperature history of the part is used as an input heat load for the mechanical model. Finite element analysis is performed using Abaqus [53], a commercially available software.

Our analysis is based on stress development in an AM part as a result of a single scan of an electron beam along its length. A layer thickness, 50 μm and a part of dimensions (in mm), $2 \times 1.5 \times 0.65$ is used as shown in Figure 3 (left). The process of laying the new powder on bulk material formed by previous scans is simulated by activating the initially deactivated elements representing the powder layer. To mitigate computational cost associated with FEA, a non-uniform mesh is employed wherein a finer mesh is considered for the powder region where the heat flux is applied. A gradually coarsening mesh is considered for the bulk material, significantly far from the heat source as shown in Figure 3 (right). The mesh consists of 13,200 nodes and 10,752 elements in total. The material used to manufacture the

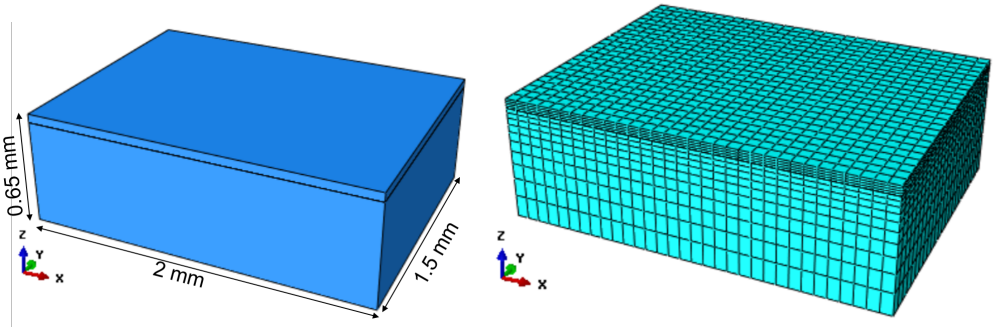

Figure 3: Part geometry and the corresponding mesh as modeled in Abaqus

part is Ti6Al4V and its thermophysical properties considered in the finite element analysis are provided in Table 1.

3.1 Thermal Model

The governing equation for the heat transfer analysis [55] is given by:

$$\rho C_p \frac{\partial T}{\partial t} = \nabla \cdot (\kappa \nabla T) + Q_e - Q_r \tag{6}$$

where T, ρ, C_p, κ, Q_e, Q_r denote the local temperature, average density, specific heat, thermal conductivity, applied heat flux and the radiative heat flux respectively. A single

Table 1: Thermophysical properties of Ti-6Al-4V [54]

Density (kg /m^3)	4428
Solidus Temperature (° C)	1605
Liquidus Temperature (° C)	1655
Latent heat (J/kg)	365000
Elastic Modulus (GPa)	110
Poisson's ratio	0.41
Yield strength (MPa)	825

scan is considered along the x-direction at the top surface of the part. Heat flux due to the moving electron beam is modeled as a Gaussian [36] according to the following equation:

$$Q_e = \frac{2P}{\pi r^2 d}\frac{1}{5}\Big[-3\Big(\frac{z}{d}\Big)^2 - 2\frac{z}{d} + 5\Big]\exp\left(\frac{-2((x-vt)^2+y^2)}{r^2}\right) \tag{7}$$

where $P = \alpha IV$ denotes the power associated with the electron beam for a given absorptivity (α), current (I), and voltage (V). The quantities: v, r, and d denote the beam velocity or scan speed, beam spot radius, and penetration depth respectively. The external heat flux is illustrated using temperature contours on the top surface in Figure 4 (left) and along x-z plane passing through the center of the part in Figure 4 (right).

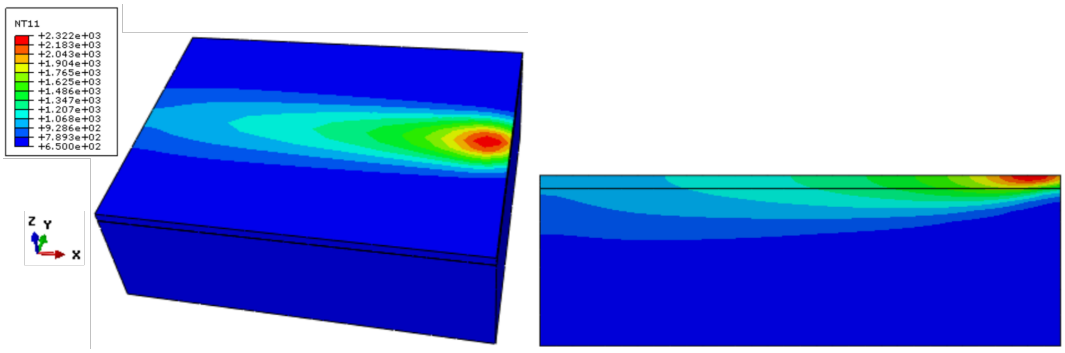

Figure 4: Left: Temperature contours associated with the moving electron beam as a heat source. Right: Temperature contours in the x-z plane passing through the center of the part once the electron beam is turned off.

The laser beam radius (r) and the thermal penetration depth are fixed at 200 and 28 microns respectively. The powder is pre-heated to a temperature, T_0 prior to the scan using fixed temperature boundary conditions at the lateral sides as well as the bottom of the part. Heat transfer in the part occurs by two mechanisms: First, by means of thermal

conduction due to temperature gradients especially along the depth (x-z plane), and second, by means of radiative losses from the exposed surface of the part denoted as Q_r in (6). The radiative heat flux, Q_r is modeled using the Stefan-Boltzmann law i.e., $Q_r = \sigma_{\text{SB}}\epsilon(T^4 - T_a^4)$, where σ_{SB}, ϵ, and T_a denote the Stefan-Boltzmann constant, emissivity of the top surface, and the ambient temperature respectively. Note that convective losses are not considered since the manufacturing process is assumed to be carried out in vacuum. As discussed later in Section 4, the beam power (P), scan speed (v), and pre-heat temperature of the powder bed (T_0) are considered as process parameters ($\boldsymbol{\theta_P}$) in our analysis using the surrogate model. The temperature history of the part determined using the thermal model is used as an input to the mechanical model (one way coupling) to compute residual stress in the AM part as discussed in the following section.

3.2 Mechanical Model

The governing equation for structural analysis [56] is given by:

$$\nabla \cdot \sigma + f = 0 \tag{8}$$

where σ denotes the stress tensor. The internal forces, f are developed within the part to be able to balance external forces. From Hooke's law, the stress tensor (σ) is proportional to the total strain (ϵ^T). Material stiffness tensor, $\mathbf{C}$ is the proportionality constant. The constitutive relationship is given as follows:

$$\sigma = \mathbf{C}\epsilon^e \tag{9}$$

where $\mathbf{C}$ is the fourth-order material stiffness tensor and ϵ^e denotes the elastic strain. The total strain ϵ^T can be decomposed as follows:

$$\epsilon^T = \epsilon^e + \epsilon^p + \epsilon^t \tag{10}$$

where ϵ^p, and ϵ^t denote plastic and thermal strains respectively [56]. The plastic strain is modeled by considering elastic perfectly-plastic [57] condition in the model. Thermal strain is calculated from the thermal expansion constitutive relationship: $\varepsilon^t = \alpha_t \Delta T$, where α_t is the thermal expansion coefficient. The boundary surfaces in the X-direction and Y-direction

are constrained in the x- coordinates and y-coordinates respectively. The bottom surface is considered fixed in all coordinates. The temperature history at each node, obtained using the thermal model in 3.1, is used to compute the strain tensor, σ. Hence, the mechanical response is dependent on the thermal response of the part but not vice versa. The coupling between the two models is therefore regarded as *one-way* or *weak* [58] (A *strong* or *two-way* coupling assumption is computationally unaffordable, since it requires multiple back-and-forth iterations between the two models for convergence, at each time step). The weak coupling does introduce approximation errors, however, it has been shown to capture experimental trends with reasonable accuracy in similar applications [59]. Moreover, the PCAS method presented in Section 2 is not impacted by this approximation.

The von Mises stress at the end of the cooling process is considered as the residual stress in the AM part [36]. It is considered as the quantity of interest (QoI) in our analysis for demonstrating the methodology proposed earlier in Section 2. The stress contours are illustrated in Figure 5 The contour plot in Figure 5 clearly indicates that the residual stress

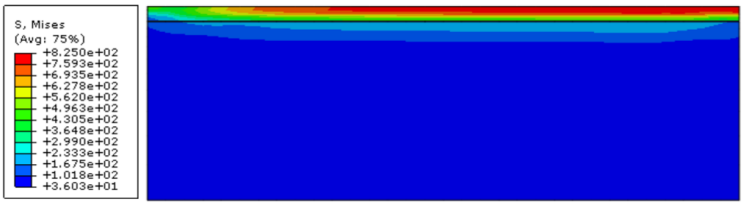

Figure 5: von Mises stress contours in the x-z plane passing through the center of the part after it has cooled down to the ambient temperature.

in the part attains higher values near the top surface and diminishes quickly along the depth of the part. It can thus be said that thermal strain due to the applied heat flux is the dominant contributor to the residual stress in the present set-up.

Simulations are performed on a workstation with a system configuration: Intel Core i7-4790 CPU, 3.60 GHz with 16GB RAM. It is observed that on average the thermal model takes 20 minutes, and the mechanical model takes 10 minutes to complete the simulation pertaining to a single pass of the electron beam. Note, however, that the simulation duration depends on the choice of values for the set of inputs. Moreover, a weak coupling assumption leads to a computational time of 30 minutes to generate 1 training point for the surrogate model.

On the other hand, a strong coupling assumption would lead to 150 minutes considering 5 iterations are needed for convergence to generate 1 training point.

4 Results

In this section, we provide relevant details pertaining to the construction of the surrogate model to predict the field quantity of interest, i.e. residual stress in a cross-section of an AM part using the PCAS method in 4.1. The computational efficiency enabled by the surrogate model is exploited for identifying stress hotspots in the part in 4.2. Note however that in addition to identifying stress hotspots, the surrogate model could be used for other quantities of interest such as mean stress, range of stress, etc., since it maps the process parameters and the material properties to the entire stress field as mentioned. Additionally, the surrogate model is used to perform a global sensitivity analysis of the inputs in 4.3. Finally, the surrogate model is used for reliability prediction of the manufactured part by estimating the probability of failure based on residual stress in 4.4.

4.1 Surrogate Model

A surrogate model is constructed for the residual stress field at the cross-section of the part (x-z plane in Figure 3) passing through its center. We will refer to this plane as x^c-z^c in the remainder of this paper. The surrogate model maps three sets of parameters, namely, the process parameters ($\boldsymbol{\theta_P}$), mechanical properties ($\boldsymbol{\theta_M}$), and thermal properties ($\boldsymbol{\theta_T}$) to the stress field. Note that the surrogate model maps a deterministic set of parameter values to a deterministic stress field. However, since the parameters are uncertain, we obtain an ensemble of such deterministic maps. In other words, the uncertainty in the parameters is propagated to obtain a distribution in the output stress field. The set of process parameters includes beam power (P), scan speed (v), and pre-heat temperature (T_0). Mechanical properties include yield strength (Y), elastic modulus (E), and bulk density (ρ). Thermal properties include specific heat (C_p) and bulk thermal conductivity (κ). Note that C_p and κ are considered to be functions of the local temperature, T. Specifically, a polynomial of degree 2 is fit to a set of data pertaining to the variation of C_p and κ with temperature

(20 K–1655 K), provided in [54] as shown in Figure 6. Hence, a total of 12 parameters ($\boldsymbol{\theta}$)

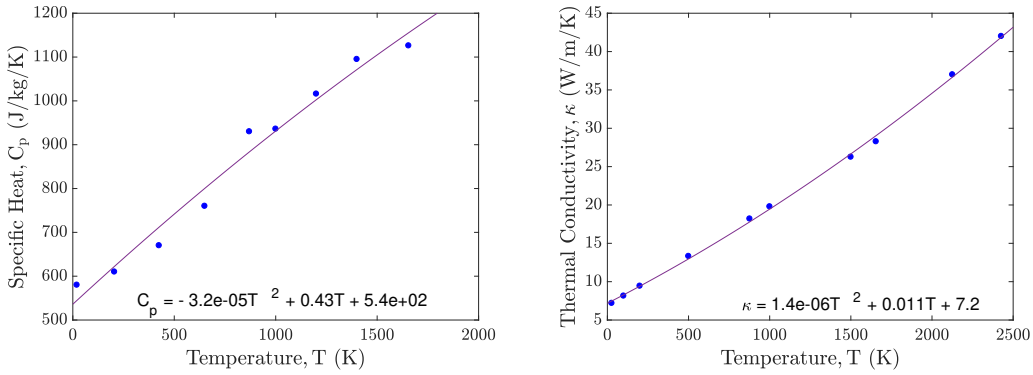

Figure 6: A second degree polynomial fit to specific heat (C_p), and thermal conductivity (κ) data for a temperature range, [20,1655](K). Note that the data provided in [54] is used to determine the coefficients of the regression fit.

are mapped to the stress field including coefficients of the polynomial fits corresponding to C_p and κ. A uniform probability distribution in a range: $[0.9\boldsymbol{\theta}^*, 1.1\boldsymbol{\theta}^*]$, where $\boldsymbol{\theta}^*$ denotes a vector of nominal values, is considered for each parameter. Nominal values of the mechanical properties: Y, E, and ρ are provided in Table 1. Nominal values of the process parameters and temperature coefficients for the thermal properties are provided in Table 2. It must be noted that the choice of a uniform probability distribution for $\boldsymbol{\theta}$ indicates that any value in the considered range for a given parameter has a probability value of $1/(u-l)$ (u: upper limit, l: lower limit) associated with it. Predictions of the original physics model at a collection of so-called training points, generated using Latin hypercube sampling (LHS) in the input probability space is used to train the surrogate model for each $\mathcal{Z}_i$ as discussed further below. Therefore, surrogate construction is purely a computational exercise in the present scenario and does not use any manufacturing data.

Table 2: EBM process parameters and temperature coefficients for C_p (C_{i,C_p}) and κ ($C_{i,\kappa}$).

Scan Speed, v (mm/s)	500
Beam Power, P (W)	160
Pre-heat Temperature, T_0 (°C)	650
Specific heat, $C_p = C_{0,C_p} + C_{1,C_p}T + C_{2,C_p}T^2$ (J/kg/K)	540 (C_{0,C_p}),0.43 (C_{1,C_p}),-3.2×10^{-5} (C_{2,C_p})
Thermal Conductivity, $\kappa = C_{0,\kappa} + C_{1,\kappa}T + C_{2,\kappa}T^2$ (W/m/K)	7.2 ($C_{0,\kappa}$),0.011 ($C_{1,\kappa}$),1.4×10^{-6} ($C_{2,\kappa}$)

Residual stress is initially computed at the x^c-z^c plane for 10 pseudorandom samples in the

12-dimensional input domain. Stress data is simulated on a 2-dimensional non-uniform grid comprising 32 points along the length (x^c) and 14 points along the height (z^c) as highlighted in Figure 10 (left). Note that the mesh size was selected such that a converged solution was obtained within a reasonable amount of computational effort. As mentioned earlier in Section 3, a finer mesh is used near the part surface since sharp thermal gradients lead to a larger amount of stress in this region as shown in Figures 5 and 10. Following the flow diagram in Figure 1, the first step involves a principal component analysis on the field data using Algorithm 1. However, the reconstructed field in this case although results in a small fitting error ($\varepsilon_0^{\text{fit}}$) of 0.06, the validation error ($\varepsilon_0^{\text{val}}$) of 0.31 is significantly larger than the set tolerance, $\tau_s = 0.1$. A new set of 5 model realizations are added in each subsequent iteration and the resulting surrogate is assessed for accuracy. The iterative procedure is observed to converge in 2 iterations. Error estimates for each iteration and the corresponding number of representative features are provided in Table 3.

Table 3: Convergence of the surrogate model as a function of iterations and sample size.

Iteration	Sample Size	# of features	$\varepsilon_i^{\text{fit}}$	$\varepsilon_i^{\text{val}}$
0	10	5	0.06	0.31
1	15	7	0.09	0.28
2	20	7	0.04	0.07

In Figure 7, we plot the reconstruction error, $\varepsilon_{\mathcal{R}}^{\infty}$ against the number of principal components K for the converged case with 20 samples. As expected, $\varepsilon_{\mathcal{R}}^{\infty}$ is observed to mostly decrease with the number of components. A monotonic behavior is not expected since the components only capture partial information in the data. It appears that all the information is captured using 20 components as the value of $\varepsilon_{\mathcal{R}}^{\infty}$ is expectedly 0 since a maximum of 20 samples were used during SVD. However, building the surrogate model for 20 features would potentially entail a large computational effort depending upon the application. Here, we consider that $K^* = 7$ corresponding to $\varepsilon_{\mathcal{R}}^{\infty} < \tau = 0.06$ as the optimal number of components. Moreover, it is observed that the error plateaus as the number of components increase from 7 to 10 indicating diminishing returns. Thus, the residual stress field is reconstructed using a surrogate model for each of these K^* components ($\mathcal{Z}_i$'s, $i = 1, 2, \ldots, K^*$). The

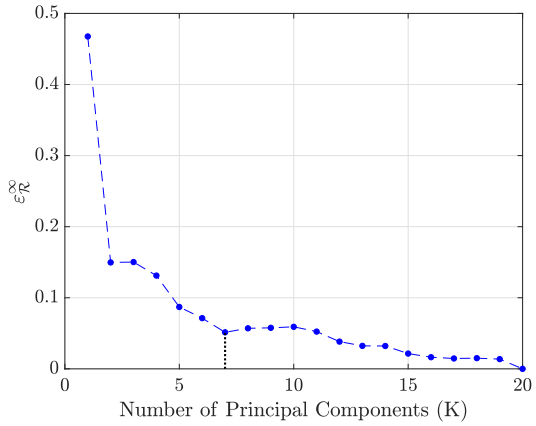

Figure 7: A plot of the reconstruction error, $\varepsilon_{\mathcal{R}}^{\infty}$ as a function of the number of principal components obtained using the iterative PCA approach in Algorithm 1 and model realizations at 20 samples.

dimensionality of the output space is therefore reduced from $\mathbb{R}^{14\times32=448} \rightarrow \mathbb{R}^{7}$. It must be noted that the choice of the thresholds, τ and τ_s is problem-dependent and it may not be possible to assume a reasonable value upfront. In this case, we mainly rely on the trends in Figure 7 to obtain a reasonable estimate of τ. In general, we suggest assuming an initial conservative guess for τ and τ_s based on desired accuracy of the reconstructed field in Algorithm 1. However, it is likely that owing to numerical approximations pertaining to PCA, gradient estimation during active subspace computation, and a surrogate-fit in the active subspace, the PCAS method might either not converge or become computationally intractable. In such a scenario, the set tolerances can be increased in an iterative manner in order to reduce the underlying computational effort. We now shift our focus on dimension reduction in the input space.

As discussed earlier in 2.2.2, each feature can be expressed as a function of $\boldsymbol{\theta} : \{\boldsymbol{\theta_P} \cup \boldsymbol{\theta_M} \cup \boldsymbol{\theta_T}\}$ in the physical space. An active subspace computation is performed using a regression-based approach [30, 48] for estimating the gradient and the available set of 20 realizations for each $\mathcal{Z}_i$. The eigenvalue spectrum of the matrix, $\hat{\mathbb{C}}_i$ for each $\mathcal{Z}_i$ is shown in Figures 8 and 9. The variability of a given $\mathcal{Z}_i$ in terms of the active variables, $\boldsymbol{\eta}$ regarded as the sufficient summary plot (SSP) is also included in each case. From these plots, it is observed that in all cases except $\mathcal{Z}_4$, a 1-dimensional active subspace captures the variability

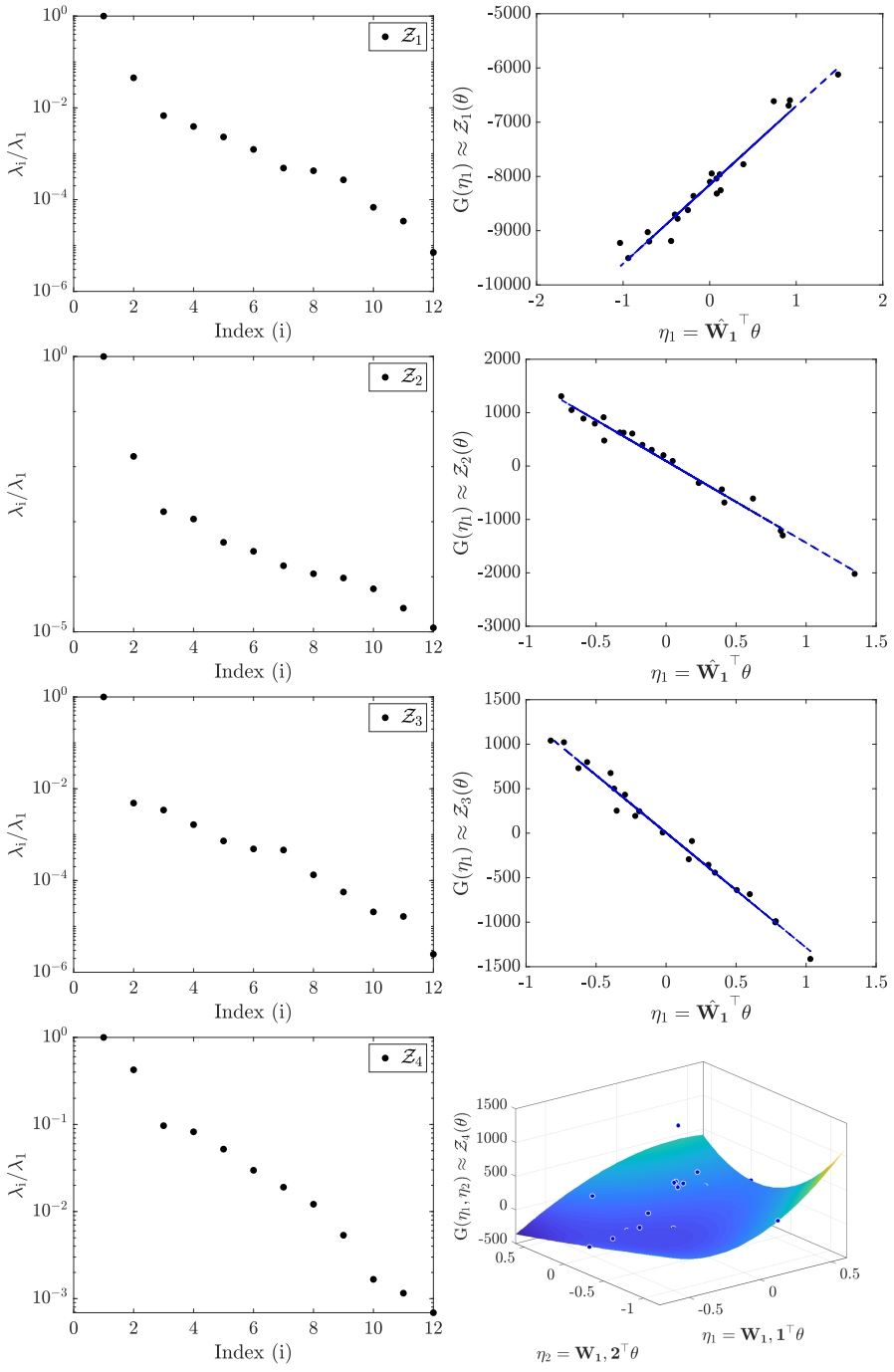

Figure 8: Eigenvalue spectrum (left) and the corresponding SSP (right) for $\mathcal{Z}_i, i = 1, 2, 3, 4$. A straight line fit in the case of $\mathcal{Z}_{1,2,3}$ and a 2D polynomial surface fit in the case of $\mathcal{Z}_4$ is used as a surrogate model as illustrated.

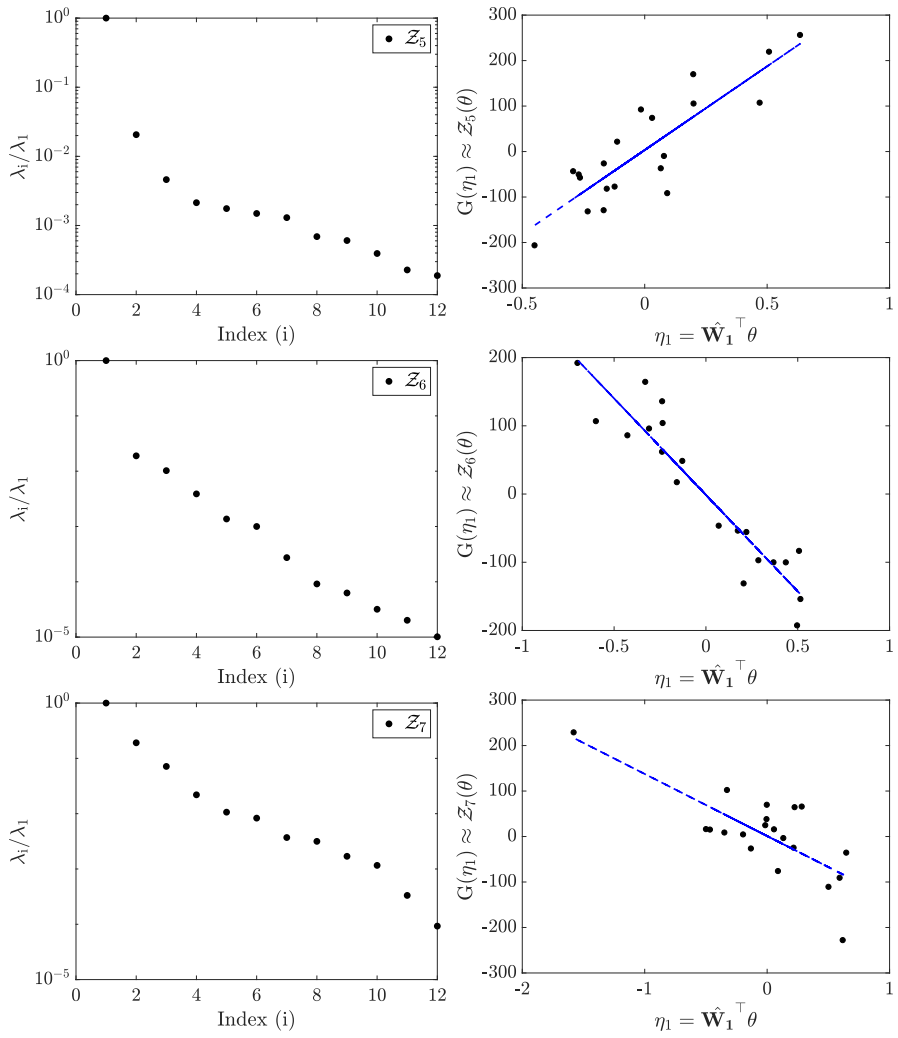

Figure 9: Eigenvalue spectrum (left) and the corresponding SSP (right) for $\mathcal{Z}_i, i = 5, 6, 7$. A straight line fit to the SSP is used as a surrogate model as illustrated in each case.

in the feature with reasonable accuracy. This is expected based on the eigenvalue spectrum which exhibits a significant jump between λ_1 and λ_2. A polynomial fit in terms of a single variable η_1 could thus be used as a surrogate model for these features. In fact, a fitting error (not reported) was computed with increasing polynomial degrees ranging from 1 to 3, and a straight-line fit was found to be most accurate in the case of $\mathcal{Z}_{i\neq 4}$. It must also be noted that higher degree polynomial fits are susceptible to over-fitting. In the case of $\mathcal{Z}_4$, λ_1 and λ_2 are observed to be comparable, and a significant jump exists between λ_2 and λ_3. Therefore, a 2-dimensional active subspace is considered in this case as shown. Polynomials of degrees 3 and 2 along η_1 and η_2 respectively were found to yield sufficient accuracy and are therefore used to construct the regression surface in this case. Therefore, a sample $\boldsymbol{\xi}_i$ corresponding to $\boldsymbol{\theta}_i$ in the physical space is propagated through each surrogate model to estimate $\mathcal{Z}_i$'s and hence, the residual stress field as shown using a flow diagram in Figure 2. The individual surrogate models for $\mathcal{Z}_i$'s thus constitute the overall surrogate model that maps the physical variables to the stress field.

Dimension reduction in the input space is thus found to be from $\mathbb{R}^7 \rightarrow \mathbb{R}^2$. Therefore, using the proposed PCAS method, significant dimension reduction in both input and output spaces is accomplished, thereby yielding enormous gains in computational efficiency for the considered application.

4.1.1 Surrogate Assessment

As mentioned earlier in this section, 20 model realizations are needed to obtain a surrogate model with reasonable accuracy with respect to the reconstructed residual stress field in the x^c-z^c plane. Specifically, the fitting and validation errors are found to be approximately 0.04 and 0.07 respectively. In other words, the mean error introduced by the surrogate model for stress field reconstruction is approximately 7%. The validation error was computed using an independent set of 10 model realizations. Although these error estimates are based on a relatively small sample size, they seem reasonable considering that the validation test samples are generated using LHS that explores the entire input domain more uniformly as compared to Monte Carlo sampling. Therefore, the PCAS approach appears to provide a reasonably accurate surrogate model coupled with enormous computational gains which

makes the analyses pertaining to the present application affordable.

Figure 10 illustrates a side-by-side comparison of stress distribution in the x^c-z^c plane, computed using the multiphysics model (left) with those generated using the surrogate model (right) using the same set of input conditions. The two plots are observed to be in close agreement with each other. Note that the stress distribution on the left generated using the finite element model took approximately 30 minutes, whereas, the surrogate model took a split second to generate the distribution on the right indicating enormous gains in computational efficiency for the considered application. Subsequent analyses such as hotspot identification, GSA, and reliability prediction presented in 4.2, 4.3, and 4.4 respectively require tens of thousands of model predictions and are therefore intractable using the original model. The proposed surrogate modeling approach is shown to make them tractable.

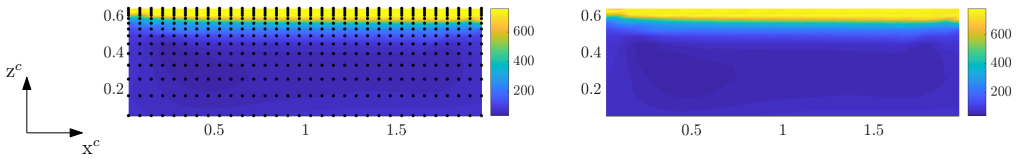

Figure 10: Left: Residual stress field in the x^c-z^c plane as generated using the finite element model in Abaqus. The grid points in the 2D mesh used in simulations are also highlighted. CPU time required to generate this plot is approximately 30 minutes. Right: Reconstructed stress field using the surrogate model using the same set of parameters. CPU time required to generate this plot is less than a second.

4.2 Hotspot Identification

As mentioned earlier in Section 1, a large amount of residual stress severely impacts part performance due to sub-optimal mechanical properties, reduced fatigue life, and geometrical inaccuracy. Identification of 'stress hotspots' is thus an important step in supporting the manufacturing process quality control. Owing to the transient nature of the process conditions, material microstructure, and part configuration, it would not be practicable to use the expensive multiphysics model for this purpose. The surrogate model constructed using the PCAS method proposed in this work is used instead.

For the present analysis, any location in the x^c-z^c plane where the residual stress exceeds a threshold is considered as a hotspot. Figure 11 illustrates the location of the hotspots

and associated stress values in the x^c-z^c plane for a particular set of input conditions using a threshold value of 640 MPa. As expected, the hotspots are located near the top surface

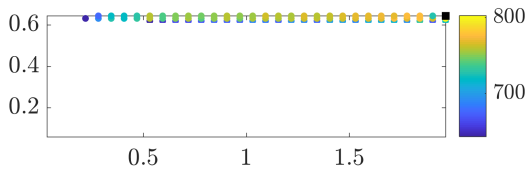

Figure 11: Location of the hotspots in the AM part and corresponding estimates of the von Mises stress are indicated by means of a colorbar. The location of the peak stress (l^*) is also shown using a black square.

of the part that experiences sharp temperature gradients. For the purpose of identifying a global hotspot, the residual stress field in the x^c-z^c plane is simulated for 10^6 pseudorandom samples, generated using LHS in the 12-dimensional input domain and projected to an active subspace corresponding to each representative feature in the stress field as shown using a flow diagram in Figure 2. Thus, stress distribution is obtained at each point in the mesh. The specific grid point with the maximum mean stress is regarded as the *global hotspot*, denoted as l^*. Our findings reveal that l^* is in fact located at the top right corner of the x^c-z^c plane, consistent with the location of the square in Figure 11. Figure 12 shows the PDF of stress distribution at point l^*.

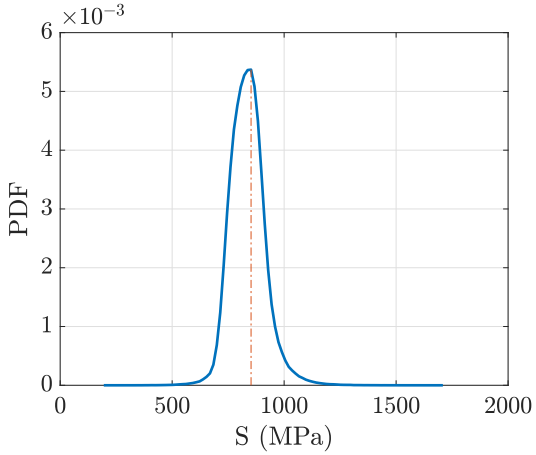

Figure 12: Probability density function (PDF) of von Mises stress at l^*, generated using kernel density estimation in Matlab. The distribution is based on 10^6 evaluations and the mode value is estimated as 852.31 MPa.

Note that Figures 11 and 12 are generated using surrogate model predictions at 10^6 samples as mentioned above. Using the physics model which requires approximately 30 minutes per run would be impractical for such analyses.

4.3 Global Sensitivity Analysis

The surrogate model is further used for the purpose of global sensitivity analysis (GSA). GSA is performed with respect to the stress value at point l^*, identified as the global hotspot for residual stress in the x^c-z^c plane as discussed earlier in 4.2.

As mentioned earlier, the set of inputs in the physical space denoted by $\boldsymbol{\theta}$ is classified into three categories: process parameters ($\boldsymbol{\theta_P}$), mechanical properties ($\boldsymbol{\theta_M}$), and thermal properties ($\boldsymbol{\theta_T}$) of the alloy (Ti6Al4V) used to manufacture the AM part. We focus our efforts on determining the relative importance of $\boldsymbol{\theta_P}$, $\boldsymbol{\theta_M}$, and $\boldsymbol{\theta_T}$ wherein the individual parameters in each category are grouped together. Additionally, we investigate the relative importance of the process parameters and the material properties, i.e. $\boldsymbol{\theta_M}$ and $\boldsymbol{\theta_T}$ grouped together. Such analyses with grouped variables would help focus the manufacturer's attention on the key contributors to the variability in residual stress. For instance, depending upon the sensitivity estimates, the manufacturer could focus on optimizing either the mechanical properties, thermal properties, or the process variables for minimizing the uncertainty in residual stress prediction. More importantly, optimizing the key contributors to the variability in residual stress would help maximize the reliability of the finished product.

GSA is performed by estimating the main-effect (S_i) and the total-effect (S_{T_i}) Sobol' sensitivity indices at 10^5 samples in the input domain using an algorithm based on Monte Carlo sampling (MCS) [60]. Mathematically, S_i and S_{T_i} can be expressed as follows:

$$S_i = \frac{\overbrace{\mathbb{V}\left(\mathbb{E}\left[f|\theta_i\right]\right)}^{\text{contribution due to } \theta_i}}{\mathbb{V}(f)}, \tag{11}$$

$$S_{T_i} = 1 - \frac{\overbrace{\mathbb{V}\left(\mathbb{E}\left[f|\boldsymbol{\theta_{\sim i}}\right]\right)}^{\text{contribution due to } \boldsymbol{\theta_{\sim i}}}}{\mathbb{V}(f)}, \tag{12}$$

where θ_i denotes the i^{th} uncertain parameter, and $\boldsymbol{\theta_{\sim i}}$ denotes a set of all uncertain parameters except θ_i. Estimating the Sobol' indices thus involves computing variance over

an expectation that is typically approximated using numerical techniques such as sampling-based methods (quadrature, Latin hypercube sampling, etc.). Model runs at a large number of sample points (especially in a high-dimensional setting) are typically needed for estimating S_i and S_{T_i} with reasonable accuracy. Therefore, in applications such as those considered in this work, it is not feasible to use simulations of an expensive physics model for this purpose. The surrogate model is therefore employed to make the computations tractable. The estimated sensitivities for the two cases are plotted in Figure 13. Several inferences can be

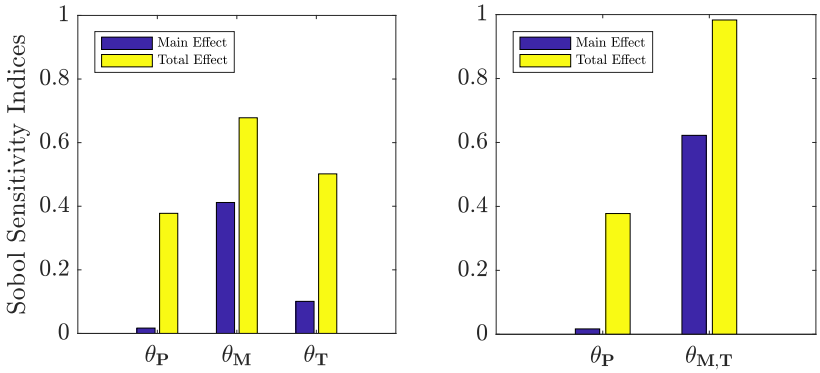

Figure 13: Left: Sobol' sensitivity indices for the set of inputs grouped as process variables ($\boldsymbol{\theta_P}$: v, P, T_0), mechanical properties ($\boldsymbol{\theta_M}$: Y, E, ρ), and thermal properties ($\boldsymbol{\theta_T}$: C_p, κ). Right: Sobol' sensitivity indices for the set of inputs grouped as process variables ($\boldsymbol{\theta_P}$), and material properties ($\boldsymbol{\theta_{M,T}}$).

made: The residual stress at P is most sensitive to the mechanical properties, followed by thermal properties of the alloy. Sensitivity towards the process parameters is found to be relatively small. Consistent with these findings, the sensitivity towards the material properties grouped together is relatively higher as compared to the process variables. However, it must be noted from these plots that the interactions between $\boldsymbol{\theta_P}$, $\boldsymbol{\theta_M}$, and $\boldsymbol{\theta_T}$ are significantly large. Hence, the total-effect index of $\boldsymbol{\theta_P}$ indicates that the sensitivity towards the process variables is significant. Therefore, optimizing the process parameters for minimizing residual stress in the AM part could help improve its performance characteristics. Note that these results are dependent on the choice of nominal values as well as considered intervals for the uncertain inputs.

The main-effect and total-effect sensitivity indices of the 12 uncertain parameters are plotted in Figure 14. Specifically, the yield strength (Y) is observed to a major contributor

to the variability in peak stress. Other important contributors include material properties, elastic modulus (E) and bulk density (ρ) as well as constants, C_{1,C_p} and $C_{1,\kappa}$ associated with the specific heat (C_p) and bulk thermal conductivity (κ) respectively. Contributions due to the process parameters, scan speed (v) and the pre-heat temperature (T_0) are also found to be significantly large. These results are found to be consistent with those presented in Figure 13. It is also observed that there is significant disparity between the main-effect and total-effect indices in all cases except for P and Y. This indicates that contribution to the variability in peak stress due to interactions among parameters is significantly large.

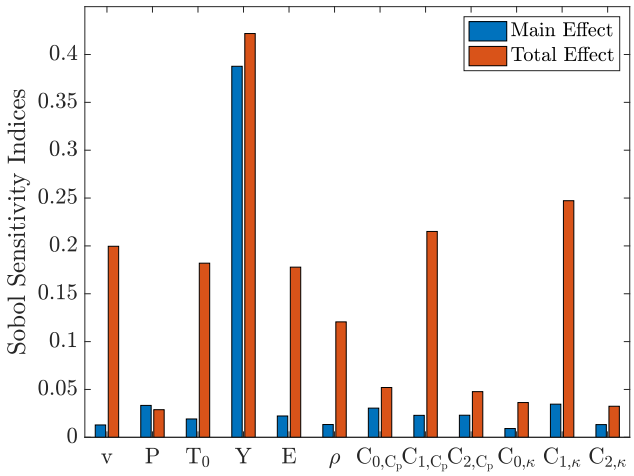

Figure 14: Sobol' sensitivity indices of the 12 uncertain parameters mapped to the stress field using the surrogate model.

From the results presented in Figure 14, it is evident that the interactions between parameters are important contributors to the variability in peak stress. Therefore in addition to the main-effect and total-effect indices, second-order (S_{ij}) Sobol' indices are estimated to gain insight into the relative contribution to stress variance by individual pairwise interactions between parameters. These insights pertaining to pairwise contributions to the variability in residual stress could also be exploited for process control and material property optimization. Considering that there are 12 uncertain parameters, a total of 66 ($^{12}C_2$) pairwise interaction terms are possible. Estimates of S_{ij} as well as are provided in Table 4. Each cell has been color coded in 'grey' with intensity based on corresponding S_{ij} estimate in

order to highlight significant interactions. Mathematically, S_{ij} can be expressed as follows:

$$S_{ij} = \frac{\overbrace{\mathbb{V}\left(\mathbb{E}\left[f|\theta_{i,j}\right]\right)}^{\text{contribution due to } \theta_{\text{i}} \text{ and } \theta_{\text{j}}}}{\mathbb{V}(f)}. \tag{13}$$

Table 4: Pairwise and total second-order Sobol' indices

	v	P	T_0	Y	E	ρ	C_{0,C_p}	C_{1,C_p}	C_{2,C_p}	$C_{0,\kappa}$	$C_{1,\kappa}$	$C_{2,\kappa}$
v		0.0002	0.0142	0.0025	0.0070	0.0080	0.0021	0.0185	0.0016	0.0019	0.0203	0.0014
P	0.0002		0.0004	0.0001	0.0000	0.0001	0.0001	0.0001	0.0000	0.0001	0.0006	0.0000
T_0	0.0142	0.0004		0.0051	0.0046	0.0106	0.0045	0.0083	0.0024	0.0044	0.0441	0.0033
Y	0.0025	0.0001	0.0051		0.0005	0.0018	0.0008	0.0017	0.0004	0.0008	0.0080	0.0006
E	0.0070	0.0000	0.0046	0.0005		0.0025	0.0004	0.0040	0.0004	0.0003	0.0043	0.0002
ρ	0.0080	0.0001	0.0106	0.0018	0.0025		0.0015	0.0074	0.0009	0.0015	0.0157	0.0011
C_{0,C_p}	0.0021	0.0001	0.0045	0.0008	0.0004	0.0015		0.0012	0.0003	0.0007	0.0069	0.0005
C_{1,C_p}	0.0185	0.0001	0.0083	0.0017	0.0040	0.0074	0.0012		0.0014	0.0008	0.0110	0.0005
C_{2,C_p}	0.0016	0.0000	0.0024	0.0004	0.0004	0.0009	0.0003	0.0014		0.0003	0.0035	0.0002
$C_{0,\kappa}$	0.0019	0.0001	0.0044	0.0008	0.0003	0.0015	0.0007	0.0008	0.0003		0.0067	0.0005
$C_{1,\kappa}$	0.0203	0.0006	0.0441	0.0080	0.0043	0.0157	0.0069	0.0110	0.0035	0.0067		0.0048
$C_{2,\kappa}$	0.0014	0.0000	0.0033	0.0006	0.0002	0.0011	0.0005	0.0005	0.0002	0.0005	0.0048	
Total	0.0777	0.0017	0.1019	0.0223	0.0242	0.0511	0.0190	0.0547	0.0114	0.0180	0.1259	0.0131

The sum total of the contribution of a given parameter θ_i^* to total variance of the peak stress by means of interactions ($S^T_{i^*j}$) with other parameters can be computed as follows:

$$S^T_{i^*j} = \sum_{j\in[1,N_\theta],j\neq i^*} S_{i^*j}. \tag{14}$$

Estimate of $S^T_{i^*j}$ for each parameter is plotted in Figure 15. From the results presented in Table 4 and Figure 15, it is observed that $C_{1,\kappa}$ exhibits large second-order interactions with v and T_0. More specifically, the interaction between T_0 and $C_{1,\kappa}$ was found to be the largest followed by the interaction between v and $C_{1,\kappa}$. Thus, the thermal conductivity (κ) contributes significantly to the stress variance by means of interactions with scan speed (v) and pre-heat temperature (T_0). Additionally, it is found that the second-order interactions exhibited by P are negligible. Note that these observations are consistent with the sensitivity results plotted in Figure 14.

4.4 Reliability Prediction

Reliability prediction involves estimating the probability of failure (p_f) of the AM part corresponding to a defined failure criterion. Here, we estimate p_f based on the residual

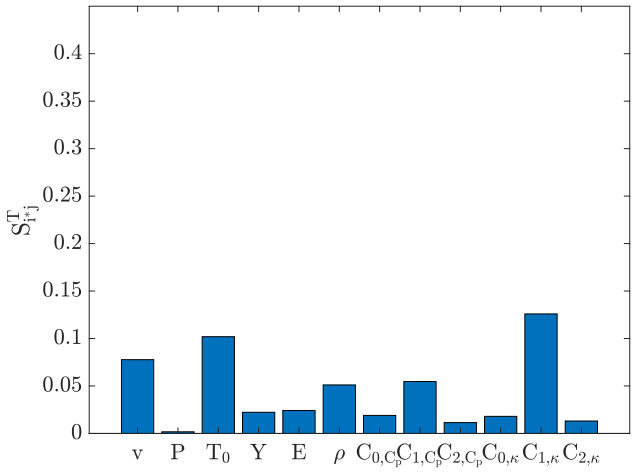

Figure 15: Estimates of $S^T_{i^*j}$ for each parameter is plotted using a bar graph.

stress estimate at any location in the part exceeding a given threshold. In other words, we aim to ensure that the residual stress in the part does not exceed an upper bound and therefore, the performance characteristics of the AM part are not severely degraded. Once again, we exploit the surrogate model to numerically estimate p_f as follows:

$$\hat{p}_f = \frac{1}{N}\sum_{k=1}^{N} \mathbb{H}\left[\max(\hat{\mathbf{S}}) - S^*\right], \tag{15}$$

where $\hat{p}_f$ is the approximation to p_f, N denotes the number of samples, S^* denotes the limiting stress value, and $\max(\hat{\mathbf{S}})$ denotes the peak stress in the x^c-z^c plane based on the surrogate model prediction. $\mathbb{H}[]$ is a Heaviside unit step function that assumes a value 1 for a positive argument and 0 for a negative argument. To ensure that $\hat{p}_f$ is a reasonable approximation, it is estimated using 10^6 samples in the input domain. Based on surrogate model predictions at these samples, the probability of failure using $S^* = 900$ MPa is estimated to be 0.177.

5 Summary and Discussion

PCA has traditionally been used for constructing reduced order models (ROMs) by mapping a field quantity to a low-dimensional orthogonal space. On the other hand, the active subspace methodology aims to identify important directions that mainly capture the variability

in a model output as a function of its inputs. Both approaches have been used extensively on an individual basis for dimensionality reduction as discussed earlier in Section 1. The main highlight of this work involves combining the two approaches in a systematic manner such that dimensionality reduction in accomplished in both input and output spaces thereby enabling enormous scope for computational gains. Specifically, we have proposed an efficient approach, namely the PCAS method for constructing a surrogate model that maps a high-dimensional input to a high-dimensional output. The high-dimensional output considered here is a field quantity, estimated at discrete points on a mesh used for numerical simulations. Computational efficiency is accomplished by means of dimension reduction in the output space as well as the input space. We begin by determining the optimal number of components required to reasonably approximate the output field using an iterative PCA approach (Algorithm 1). Variability in each feature due to the variability in the inputs is next captured in a low-dimensional subspace using the active subspace methodology. The PCAS method thus reduces the dimensionality of the map from a large set of input variables to a high-dimensional field quantity of interest. Computational efficiency is enhanced by approximating the variability of each feature in the active subspace by a low-dimensional surrogate model. The overall surrogate model that maps input variables to the output field is constructed in an iterative manner to avoid unnecessary realizations of the stress field using the expensive multiphysics model for generating the training data. It is expected that the computational efficiency is accompanied with a trade-off in accuracy. Therefore, it is critical to perform a robust assessment of the resulting surrogate model as discussed in 4.1.1.

The proposed methodology is demonstrated using an engineering application pertaining to reliability analysis of an additively manufactured part. Specifically, we focus our efforts on predicting the development of residual stress in a part at the end of an electron beam melting process using a finite element model in Abaqus. The von Mises stress field in a 2-dimensional non-uniform mesh in a cross-section of the part is computed, and it is found that 7 features are able to approximate the stress field using the iterative PCA approach. The set of inputs comprising the process parameters, and mechanical and thermal properties of the alloy (used to manufacture the AM part) are mapped to each of these 7 features. A 1-or-2 dimensional active subspace is shown to reasonably capture the dependence of each feature on the inputs

thereby indicating enormous scope for computational gains. The surrogate model is shown to be remarkably accurate by estimating the relative L-2 norm of the discrepancy between the model output and the field reconstructed using the surrogate model. Specifically, on average, the fitting error and the validation error are found to be approximately 4% and 7% respectively.

The surrogate model is used for identifying stress hotspots in an AM part in 4.2, and global sensitivity analysis of the process variables, mechanical, and thermal properties of the alloy in 4.3. The hotspots are observed to be in the proximity of the applied heat flux by the electron beam, i.e. closer to the surface of the AM part. This clearly indicates that the residual stress is dominated by the presence of large temperature gradients. The GSA results highlight that the residual stress is relatively more sensitive to the material properties, although the sensitivity towards the process variables is also found to be significant due to their interactions with the material properties; such interaction is accounted for in the total-effect index. Specifically, our computations of the second-order Sobol' sensitivity index indicate that the scan speed (v) and the pre-heat temperature (T_0) contribute significantly to the variability in peak stress through interactions with the coefficient of temperature ($C_{1,\kappa}$) used in the thermal conductivity model as provided in Table 2. Finally, the surrogate model is exploited to numerically estimate the probability of failure using a million samples in the input domain for the purpose of reliability analysis of the AM part.

It must be highlighted that the aforementioned analyses such as hotspot detection, GSA, and reliability prediction under various process and material uncertainties are typically computationally intensive in additive manufacturing. The surrogate model constructed using the PCAS method makes them computationally affordable while ensuring a reasonable amount of accuracy for the present application. In addition to the analyses presented in this work, the surrogate model-based predictions of the stress field could be used to estimate other quantities of interest such as the difference between maximum and minimum local stress, identification of regions with stress concentration in the part and so on. Furthermore, common approaches to process control in additive manufacturing are mainly based on trial-and-error with no ability to perform reliability analysis on either the part or the process. The fast surrogate modeling approach presented in this work could enable reliability analy-

sis in this rapidly emerging area. Moreover, computational efficiency enabled by dimension reduction could enable real-time process control which can otherwise be remarkably challenging. However, there are limitations that should be considered when applying the proposed methodology. First, dimension reduction in the output space is conditioned on the existence of a structure in the data that could be captured by a relatively small number of principal components or directions. Second, a low-dimensional active subspace is used here to map the set of inputs to the quantity of interest (QoI). To accomplish this effectively, the gradient of the QoI with respect to each input should be estimated with reasonable accuracy. For the application presented in this work, we have used a regression-based approach for estimating the gradients that resulted in a reasonably accurate surrogate model for each feature of the output field of interest. However, depending upon the relationship between the QoI and the set of inputs, a relatively more accurate (but expensive) approach such as those involving perturbation techniques (e.g. automatic differentiation [51], adjoint methods [49,50]) may be required. Additionally, the active subspace methodology is not suitable in situations where the QoI exhibits large nonlinearities with respect to uncertain inputs, and the gradient is not continuous in the entire domain of the inputs.

To sum up, the proposed methodology is successfully demonstrated in this paper for a reasonably challenging practical application involving reliability analysis of an additively manufactured part. Enormous computational gains leading to significant dimension reduction in both input and output spaces are accomplished. Therefore, the proposed framework appears to be quite promising for surrogate modeling in applications involving large input and output dimensions. Potential future efforts pertaining to this work could explore alternate strategies such as adjoint-based methods for gradient estimation to enhance the robustness and applicability of the proposed approach to more complex scenarios. Additionally, such improvements could enhance the applicability of the surrogate model for process control and optimization in additive manufacturing. In this work, the accuracy of the surrogate model is validated against finite-element based numerical simulations. However, for such practical applications, surrogate-based predictions must be validated against measurements in order to assess its applicability.

Acknowledgment

This study was supported by funds from the National Institute of Standards and Technology under the Smart Manufacturing Data Analytics Project (Cooperative Agreement No. 70NANB14H036, Project Monitor: Simon Frechette). The support is gratefully acknowledged.

Disclaimer

Certain commercial systems are identified in this paper. Such identification does not imply recommendation or endorsement by NIST; nor does it imply that the products identified are necessarily the best available for the purpose. Further, any opinions, findings, conclusions, or recommendations expressed in this material are those of the authors and do not necessarily reflect the views of NIST or any other supporting U.S. government or corporate organizations.

References

[1] D. Xiu, G. Karniadakis, The Wiener–Askey polynomial chaos for stochastic differential equations, SIAM Journal on Scientific Computing 24 (2) (2002) 619–644.

[2] R. Ghanem, P. Spanos, Stochastic Finite Elements: A spectral approach, Springer, 2003, pp. 101–119.

[3] O. Le Maître, O. Knio, Spectral methods for uncertainty quantification: with applications to computational fluid dynamics, Springer Science & Business Media, 2010.

[4] T. Gerstner, M. Griebel, Numerical integration using sparse grids, Numerical Algorithms 18 (3-4) (1998) 209.

[5] B. Ganapathysubramanian, N. Zabaras, Sparse grid collocation schemes for stochastic natural convection problems, Journal of Computational Physics 225 (1) (2007) 652–685.

[6] G. Blatman, B. Sudret, Adaptive sparse polynomial chaos expansion based on least angle regression, Journal of Computational Physics 230 (6) (2011) 2345–2367.

[7] P. Conrad, Y. Marzouk, Adaptive smolyak pseudospectral approximations, SIAM Journal on Scientific Computing 35 (6) (2013) A2643–A2670.

[8] C. Rasmussen, Gaussian processes in machine learning, in: Advanced lectures on machine learning, Springer, 2004, pp. 63–71.

[9] C. Cortes, V. Vapnik, Support-vector networks, Machine learning 20 (3) (1995) 273–297.

[10] S. Haykin, Neural Networks, Vol. 2, Prentice hall New York, 1994.

[11] K. Petvipusit, A. Elsheikh, T. Laforce, P. King, M. Blunt, Robust optimisation of CO_2 sequestration strategies under geological uncertainty using adaptive sparse grid surrogates, Computational Geosciences 18 (5) (2014) 763–778.

[12] A. Elsheikh, I. Hoteit, M. Wheeler, Efficient Bayesian inference of subsurface flow models using nested sampling and sparse polynomial chaos surrogates, Computer Methods in Applied Mechanics and Engineering 269 (2014) 515–537.

[13] G. Zhang, D. Lu, M. Ye, M. Gunzburger, C. Webster, An adaptive sparse-grid high-order stochastic collocation method for Bayesian inference in groundwater reactive transport modeling, Water Resources Research 49 (10) (2013) 6871–6892.

[14] X. Ma, N. Zabaras, An efficient Bayesian inference approach to inverse problems based on an adaptive sparse grid collocation method, Inverse Problems 25 (3) (2009) 035013.

[15] J. Wang, N. Zabaras, Using Bayesian statistics in the estimation of heat source in radiation, International Journal of Heat and Mass Transfer 48 (1) (2005) 15–29.

[16] D. Galbally, K. Fidkowski, K. Willcox, O. Ghattas, Non-linear model reduction for uncertainty quantification in large-scale inverse problems, International Journal for Numerical Methods in Engineering 81 (12) (2010) 1581–1608.

[17] Y. Marzouk, H. Najm, Dimensionality reduction and polynomial chaos acceleration of Bayesian inference in inverse problems, Journal of Computational Physics 228 (6) (2009) 1862–1902.

[18] P. Constantine, M. Eldred, E. Phipps, Sparse pseudospectral approximation method, Computer Methods in Applied Mechanics and Engineering 229 (2012) 1–12.

[19] J. Winokur, P. Conrad, I. Sraj, O. Knio, A. Srinivasan, W. Thacker, Y. Marzouk, M. Iskandarani, A priori testing of sparse adaptive polynomial chaos expansions using an ocean general circulation model database, Computational Geosciences 17 (6) (2013) 899–911.

[20] M. Vohra, X. Huan, T. Weihs, O. Knio, Design analysis for optimal calibration of diffusivity in reactive multilayers, Combustion Theory and Modelling 21 (6) (2017) 1023–1049.

[21] V. Hombal, S. Mahadevan, Surrogate modeling of 3D crack growth, International Journal of Fatigue 47 (2013) 90–99.

[22] P. Nath, Z. Hu, S. Mahadevan, Sensor placement for calibration of spatially varying model parameters, Journal of Computational Physics 343 (2017) 150–169.

[23] L. Borgman, R. Frahme, A case study: Multivariate properties of bentonite in northeastern Wyoming, in: Advanced Geostatistics in the mining industry, Springer, 1976, pp. 381–390.

[24] B. Davis, K. Greenes, Estimation using spatially distributed multivariate data: an example with coal quality, Journal of the International Association for Mathematical Geology 15 (2) (1983) 287–300.

[25] D. Myers, Matrix formulation of co-kriging, Journal of the International Association for Mathematical Geology 14 (3) (1982) 249–257.

[26] C. Gogu, J.-C. Passieux, Efficient surrogate construction by combining response surface methodology and reduced order modeling, Structural and Multidisciplinary Optimization 47 (6) (2013) 821–837.

[27] O. Zahm, P. Constantine, C. Prieur, Y. Marzouk, Gradient-based dimension reduction of multivariate vector-valued functions, arXiv preprint arXiv:1801.07922.

[28] W. Ji, J. Wang, O. Zahm, Y. Marzouk, B. Yang, Z. Ren, C. Law, Shared low-dimensional subspaces for propagating kinetic uncertainty to multiple outputs, Combustion and Flame 190 (2018) 146–157.

[29] P. Constantine, E. Dow, Q. Wang, Active subspace methods in theory and practice: applications to kriging surfaces, SIAM Journal on Scientific Computing 36 (4) (2014) A1500–A1524.

[30] P. Constantine, Active subspaces: Emerging ideas for dimension reduction in parameter studies, Vol. 2, SIAM, 2015.

[31] P. Withers, H. Bhadeshia, Residual stress. part 2–Nature and origins, Materials Science and Technology 17 (4) (2001) 366–375.

[32] P. Mercelis, J.-P. Kruth, Residual stresses in selective laser sintering and selective laser melting, Rapid Prototyping Journal 12 (5) (2006) 254–265.

[33] D. Hofmann, S. Roberts, R. Otis, J. Kolodziejska, R. Dillon, J. Suh, A. Shapiro, Z.-K. Liu, J.-P. Borgonia, Developing gradient metal alloys through radial deposition additive manufacturing, Scientific reports 4 (2014) 5357.

[34] F. Kim, S. Moylan, Literature review of metal additive manufacturing defects, Tech. rep. (2018).

[35] M. Shiomi, K. Osakada, K. Nakamura, T. Yamashita, F. Abe, Residual stress within metallic model made by selective laser melting process, CIRP Annals-Manufacturing Technology 53 (1) (2004) 195–198.

[36] G. Vastola, G. Zhang, Q. Pei, Y.-W. Zhang, Controlling of residual stress in additive manufacturing of Ti6Al4V by finite element modeling, Additive Manufacturing 12 (2016) 231–239.

[37] N. Hodge, R. Ferencz, R. Vignes, Experimental comparison of residual stresses for a thermomechanical model for the simulation of selective laser melting, Additive Manufacturing 12 (2016) 159–168.

[38] R. Williams, C. Davies, P. Hooper, A pragmatic part scale model for residual stress and distortion prediction in powder bed fusion, Additive Manufacturing 22 (2018) 416 – 425.

[39] K. Phoon, S. Huang, S. Quek, Simulation of second-order processes using karhunen–loeve expansion, Computers & Structures 80 (12) (2002) 1049–1060.

[40] K. Phoon, H. Huang, S. Quek, Simulation of strongly non-Gaussian processes using karhunen–loeve expansion, Probabilistic Engineering Mechanics 20 (2) (2005) 188–198.

[41] R. Ghanem, Ingredients for a general purpose stochastic finite elements implementation, Computer Methods in Applied Mechanics and Engineering 168 (1) (1999) 19–34.

[42] H. Matthies, A. Keese, Galerkin methods for linear and nonlinear elliptic stochastic partial differential equations, Computer Methods in Applied Mechanics and Engineering 194 (12-16) (2005) 1295–1331.

[43] E. Vanmarcke, Random fields: analysis and synthesis, World Scientific, 2010.

[44] J. Ramsay, B. Silverman, Applied functional data analysis: methods and case studies, Springer, 2007.

[45] K. Atkinson, The numerical solution of integral equations of the second kind (1996).

[46] W. Betz, I. Papaioannou, D. Straub, Numerical methods for the discretization of random fields by means of the karhunen–loève expansion, Computer Methods in Applied Mechanics and Engineering 271 (2014) 109–129.

[47] C.-C. Li, A. Der Kiureghian, Optimal discretization of random fields, Journal of Engineering Mechanics 119 (6) (1993) 1136–1154.

[48] M. Vohra, S. Mahadevan, Discovering the active subspace for efficient UQ of molecular dynamics simulations of phonon transport in silicon, International Journal of Heat and Mass Transfer 132 (2019) 577 – 586.

[49] A. Borzì, V. Schulz, Computational optimization of systems governed by partial differential equations, SIAM, Philadelphia, PA, USA, 2011.

[50] A. Alexanderian, N. Petra, G. Stadler, O. Ghattas, Mean-variance risk-averse optimal control of systems governed by PDEs with random parameter fields using quadratic approximations, SIAM/ASA J. Uncertainty Quantif. 5 (2017) 1166–1192.

[51] A. Kiparissides, S. Kucherenko, A. Mantalaris, E. Pistikopoulos, Global sensitivity analysis challenges in biological systems modeling, Ind. Eng. Chem. Res. 48 (2009) 7168–7180.

[52] P. Constantine, A. Doostan, Time-dependent global sensitivity analysis with active subspaces for a lithium ion battery model, Statistical Analysis and Data Mining: The ASA Data Science Journal 10 (5) (2017) 243–262.

[53] Hibbitt, Karlsson, Sorensen, ABAQUS/Standard user's manual, Vol. 1, Hibbitt, Karlsson & Sorensen, 2001.

[54] C. Fu, Y. Guo, 3-dimensional finite element modeling of selective laser melting Ti-6Al-4V alloy, in: 25th Annual International Solid Freeform Fabrication Symposium, 2014.

[55] A. Zinoviev, O. Zinovieva, V. Ploshikhin, V. Romanova, R. Balokhonov, Evolution of grain structure during laser additive manufacturing. simulation by a cellular automata method, Materials & Design 106 (2016) 321–329.

[56] M. Megahed, H.-W. Mindt, N. N'Dri, H. Duan, O. Desmaison, Metal additive-manufacturing process and residual stress modeling, Integrating Materials and Manufacturing Innovation 5 (1) (2016) 4.

[57] X. Zhao, P. Promoppatum, S.-C. Yao, Numerical modeling of non-linear thermal stress in direct metal laser sintering process of titanium alloy products, in: Proceedings of the First Thermal and Fluids Engineering Summer Conference, 2015, pp. 9–12.

[58] T. DebRoy, W. Zhang, J. Turner, S. Babu, Building digital twins of 3D printing machines, Scripta Materialia 135 (2017) 119–124.

[59] P. Farahmand, R. Kovacevic, An experimental–numerical investigation of heat distribution and stress field in single-and multi-track laser cladding by a high-power direct diode laser, Optics & Laser Technology 63 (2014) 154–168.

[60] I. Sobol, Global sensitivity indices for nonlinear mathematical models and their Monte Carlo estimates, Mathematics and Computers in Simulation 55 (1-3) (2001) 271–280.